

Article

# Fe<sub>2</sub>O<sub>3</sub> Blocking Layer Produced by Cyclic Voltammetry Leads to Improved Photoelectrochemical Performance of Hematite Nanorods

Mahshid Poornajar<sup>1</sup>, Nhat Truong Nguyen<sup>1</sup>, Hyo-Jin Ahn<sup>1,2</sup>, Markus Büchler<sup>3</sup>, Ning Liu<sup>1</sup>, Stepan Kment<sup>2</sup>, Radek Zboril<sup>2</sup>, Jeong Eun Yoo<sup>1</sup> and Patrik Schmuki<sup>1,2,4,\*</sup>

- <sup>1</sup> Department of Materials Science and Engineering, University of Erlangen-Nuremberg, Martensstrasse 7, 91058 Erlangen, Germany; mahshid.poornajar@fau.de (M.P.); nhat.truong.nguyen@fau.de (N.T.N.); Hyo-Jin.ahn@fau.de (H.-J.A.); ning.liu@ww.uni-erlangen.de (N.L.); jeong.e.yoo@ww.uni-erlangen.de (J.E.Y.)  
<sup>2</sup> Regional Center of Advanced Technologies and Materials, Šlechtitelů 27, 779 00 Olomouc, Czech Republic; stepan.kment@upol.cz (S.K.); radek.zboril@upol.cz (R.Z.)  
<sup>3</sup> Schweizerische Gesellschaft für Korrosionsschutz (SGK) Swiss Society for Corrosion Protection, Technoparkstrasse.1, CH-8005 Zürich, Switzerland; markus.buechler@sgk.ch  
<sup>4</sup> Department of Chemistry, King Abdulaziz University, 80203 Jeddah, Saudi Arabia  
\* Correspondence: schmuki@ww.uni-erlangen.de

Received: 31 December 2018; Accepted: 8 February 2019; Published: 19 February 2019



**Abstract:** Hematite is a low band gap, earth abundant semiconductor and it is considered to be a promising choice for photoelectrochemical water splitting. However, as a bulk material its efficiency is low because of excessive bulk, surface, and interface recombination. In the present work, we propose a strategy to prepare a hematite ( $\alpha$ -Fe<sub>2</sub>O<sub>3</sub>) photoanode consisting of hematite nanorods grown onto an iron oxide blocking layer. This blocking layer is formed from a sputter deposited thin metallic iron film on fluorine doped tin oxide (FTO) by using cyclic voltammetry to fully convert the film into an anodic oxide. In a second step, hematite nanorods (NR) are grown onto the layer using a hydrothermal approach. In this geometry, the hematite sub-layer works as a barrier for electron back diffusion (a blocking layer). This suppresses recombination, and the maximum of the incident photon to current efficiency is increased from 12% to 17%. Under AM 1.5 conditions, the photocurrent density reaches approximately 1.2 mA/cm<sup>2</sup> at 1.5 V vs. RHE and the onset potential changes to 0.8 V vs. RHE (using a Zn-Co co-catalyst).

**Keywords:** hematite; cyclic voltammetry; photoelectrochemical performance; oxygen evolution reaction (OER) catalyst; nanorods

## 1. Introduction

Photoelectrochemical (PEC) solar energy conversion (mimicking artificial photosynthesis) has been investigated for several decades [1]. Many metal oxide semiconductors such as TiO<sub>2</sub>, WO<sub>3</sub> and Fe<sub>2</sub>O<sub>3</sub> have been intensively studied for photoelectrochemical applications in order to generate hydrogen from water [2–6]. Hematite ( $\alpha$ -Fe<sub>2</sub>O<sub>3</sub>) as an n-type semiconductor has inherent advantages for a use as a photoanode in solar water splitting. Hematite has a narrow band gap (2.1 eV) that can use a large portion of the visible light region of the solar spectrum. It also has a valence band edge position that enables oxygen evolution, i.e., it is situated, in energy, anodic to the O<sup>2-</sup>/O<sub>2</sub> redox potential. Hematite is abundant in nature, of low cost, it is stable and provides environmental compatibility [7,8]. Despite the promising characteristics, hematite bulk electrodes have a low PEC performance, which is caused by a low hole diffusion length and a hampered hole transfer to an aqueous electrolyte. To illustrate this, the light penetration depth in  $\alpha$ -Fe<sub>2</sub>O<sub>3</sub> is about 118 nm at  $\lambda = 550$  nm [9]. However,

the hole diffusion length of hematite is only about 2–4 nm [10]. Therefore, most holes recombine before they reach the surface, i.e., only the holes which are created within the hole diffusion length near the electrolyte interface can trigger a water oxidation reaction [11]. It should be also noted that the conduction band edge of hematite is lower than the  $H^+/H_2$  redox potential, hence direct photocatalysis is not possible, and external bias and a counter electrode are needed for hydrogen evolution [12,13].

To tackle the problem of the low hole diffusion length, many kinds of nanostructures have been successfully used, such as nanotubes [14,15], nanoflakes [16,17], nanobelts [18], nanowires [19,20], nanocorals [21] and nanorods [22]. In these 1-dimensional (1D) nanostructures, the light absorption length can be tuned by the length of the nanostructure, while the hole diffusion distance to the surface is short enough for holes to reach the surface. Moreover, electrons can be transported directly to the back contact. For many 1D hematite structures their basal planes are oriented perpendicularly to the substrate, which is beneficial for a charge transfer to the substrate [18,23].

A large variety of different synthesis procedures have been used for preparing hematite nanostructures. One approach is anodization which allows synthesizing self-organizing nanostructures, such as nanotubes, on a Fe metal substrate [24–27]. Another method is thermal oxidation of iron, which is simple and cheap [28,29], and where hematite nanowhiskers and nanowires can be grown from metal substrates. However, in all these procedures, where iron foils are used as a substrate, during a subsequent annealing step in air, sub-oxides—namely  $Fe_3O_4$ —are produced at the metal/oxide interface. This  $Fe_3O_4$  interface layer is highly detrimental for the charge transfer to the substrate. One way to overcome this problem is growing full hematite nanostructures on a FTO substrate, using for instance a hydrothermal method [30–34]. As here no metallic Fe is used, undesired iron oxide phases cannot be formed upon annealing under the hematite nanostructure.

Usually pristine hematite shows a high onset potential for water oxidation. The onset potential can be reduced by adding a catalyst to the surface of the sample. For example Zn-Co layered double hydroxide (LDHs) have been considered as an excellent OER catalyst [35].

One challenge of using bare FTO as a substrate for the hydrothermal growth of hematite nanorods is that in the spaces between the nanorods interfacial recombination can take place, since there is the possibility of electron back flow into the electrolyte on the none-covered area, i.e., on FTO directly exposed to the electrolyte [36–38]. There have been some efforts for suppressing the back injection of electrons, such as introducing blocking layers between hematite and FTO substrate [39]. Such a blocking layer should be thin enough to enable electron tunneling from hematite nanorods to the FTO as illustrated in Figure 1. As an example, Hisatomi et al. reported a 2 nm  $Nb_2O_5$  buffer layer between hematite and the FTO substrate to reduce recombination at the interface of the semiconductor and the substrate [40]. Abel et al. [41] successfully investigated thin films (10–20 nm) of  $TiO_2$  on FTO. They investigated hematite thin films made by a successive ionic layer adsorption and reaction (SILAR) method, with and without  $TiO_2$  underlayer on the FTO. In this work, by annealing the samples at 775 °C, the onset potential in J-V curve of hematite with  $TiO_2$  layer shifts to more positive potential, and the current density increases from 0.21 mA/cm<sup>2</sup> to 0.35 mA/cm<sup>2</sup> at 1.4 V vs. RHE. Ferial et al. electrodeposited 40 nm to 60 nm hematite on FTO, underneath a hydrothermally fabricated hematite photoanode, and found an increase in the photoelectrochemical properties [42]. Cho et al. added 40 nm dense layer of different materials, such as  $SnO_2$  and  $Fe_2O_3$ -Ti, between hematite and the FTO substrate, which shifted the dark current onset potential to more positive values and also increased the current density [36]. Liang et al. showed that for hematite layers prepared by spray pyrolysis method the photocurrent density can be enhanced to 0.37 mA/cm<sup>2</sup> at 1.23 V vs. RHE using 5 nm  $SnO_2$  interfacial layer between hematite and FTO [43]. Hisatomi et al. have investigated ultra-thin layer (of  $Ga_2O_3$  between hematite and FTO prepared by ALD). For a 2 nm  $Ga_2O_3$  layer and a 25 nm hematite layer the photocurrent density was improved from 0.2 to 0.4 mA/cm<sup>2</sup> at 1.23 V vs. RHE [44]. Within the present work, we describe a novel form of establishing a fully adjustable blocking layer of hematite on FTO. For this, we sputtered a thin metallic iron layer on FTO and then converted this layer fully to FeOOH by an optimized cyclic voltammetry protocol [45]. This layer then can be annealed to obtain

a pure thin hematite layer on FTO. Afterwards,  $\text{Fe}_2\text{O}_3$  nanorods can be grown on the substrate by a hydrothermal procedure. We show that such nanostructured surfaces provide higher photocurrents than the same nanostructures without blocking layers. The photoelectrochemical properties can be further improved by decorating the hematite nanostructure with Zn-Co LDH, yielding a plateau photocurrent at  $1.2 \text{ mA/cm}^2$  at  $1.5 \text{ V}$  and an onset potential at  $0.8 \text{ V}$  vs. RHE.

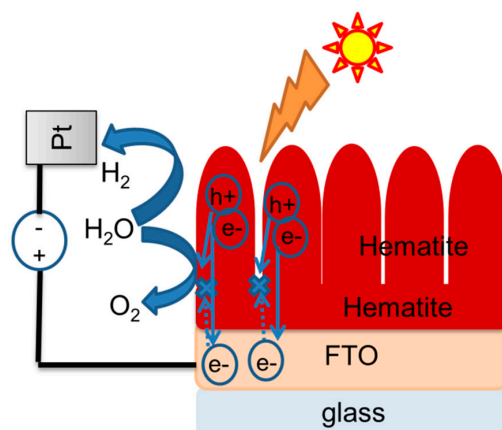


**Figure 1.** Schematic of the electron back transfer pathway and the effect of blocking layer on suppressing electron back transfer and recombination.

## 2. Materials and Methods

### 2.1. Materials Fabrication

The fabrication process of the hematite photoanodes is schematically illustrated in Figure 2. First, a layer of metallic Fe was sputter-deposited on FTO. Iron films with various thicknesses were deposited by DC pulsed magnetron sputtering. A 3" iron target (purity 99%, Lesker) and argon atmosphere were used as the source of iron and working gas, respectively. The films were deposited on FTO coated glass substrates (Solaronix). Before the deposition, the samples were cleaned by rinsing the bare FTO substrates in an ultrasound bath in a sequence of acetone, ethanol and distilled water for 10 min for each step. The substrates were then dried by a nitrogen flow. The samples were placed in an ultra-high vacuum chamber on a rotating substrate holder. A combination of rotary and turbomolecular pumps evacuated the chamber to the base pressure of  $10 \times e^{-5} \text{ Pa}$ . The working pressure during the deposition was set to  $0.9 \text{ Pa}$  by the flow rate of  $\text{Ar} = 30 \text{ sccm}$ . The deposition of iron was carried out with the applied DC power of  $650 \text{ W}$  using a pulsed mode with the pulse frequency of  $100 \text{ Hz}$  and duty cycle of  $1 \%$ . The deposition typically lasted 30 min.

The metallic layer was converted to  $\text{FeOOH}$  by cyclic voltammetry (see details below) and subsequently further oxidized to hematite by annealing at  $400 \text{ }^\circ\text{C}$  for 1 h in air. Onto this surface, hematite nanorods were grown by a hydrothermal procedure described below. Subsequently the entire structure was annealed at  $800 \text{ }^\circ\text{C}$  for 15 min to convert the as-synthesized material consisting of iron oxy-hydroxide into hematite.

Conversion of the metallic sputter-deposited thin layer into an oxide was carried out in  $0.1 \text{ M}$   $\text{NaOH}$  (reagent grade) with  $\text{pH} 13$  at the room temperature. The electrolyte was continuously deaerated by nitrogen bubbling. The solution was stirred using a magnet stirrer to remove the dissolution products from the vicinity of the electrode. The potential was measured against a  $\text{Ag}/\text{AgCl}$  reference electrode and a platinum wire was used as a counter electrode. Cyclic voltammetry was carried out using a Zahner IM6 system (Zahner Elektrik, Kronach, Germany) in a potential window from  $-1.256 \text{ V}$  vs.  $\text{Ag}/\text{AgCl}$  to  $+0.6 \text{ V}$  vs.  $\text{Ag}/\text{AgCl}$  with a sweep rate of  $5 \text{ mV/s}$ . After the CV treatment, the samples were annealed at  $400 \text{ }^\circ\text{C}$  in air for 1 h to convert the  $\text{FeOOH}$  layer formed during polarization to  $\alpha\text{-Fe}_2\text{O}_3$  (the blocking layer). For the hydrothermal synthesis procedure, iron chloride hexahydrate ( $\text{FeCl}_3 \cdot 6\text{H}_2\text{O}$ ) and titanium chloride ( $\text{TiCl}_3$ ) were used as reagents. FTO which was coated with the

hematite blocking layer as well as bare cleaned pieces of FTO glass substrate were put into a cap sealed glass bottle which was filled with 0.02 mL of 150 M  $\text{FeCl}_3 \cdot 6\text{H}_2\text{O}$  aqueous solution mixed with 8  $\mu\text{L}$  of  $\text{TiCl}_3$  and placed into the oven at 100 °C for 1, 3 and 9 h. Subsequently, a yellowish layer of iron oxyhydroxide ( $\beta\text{-FeOOH}$ ) film was grown on the substrate. The samples were washed with DI water to remove all residuals, dried in nitrogen stream, and annealed at 800 °C for 15 min.

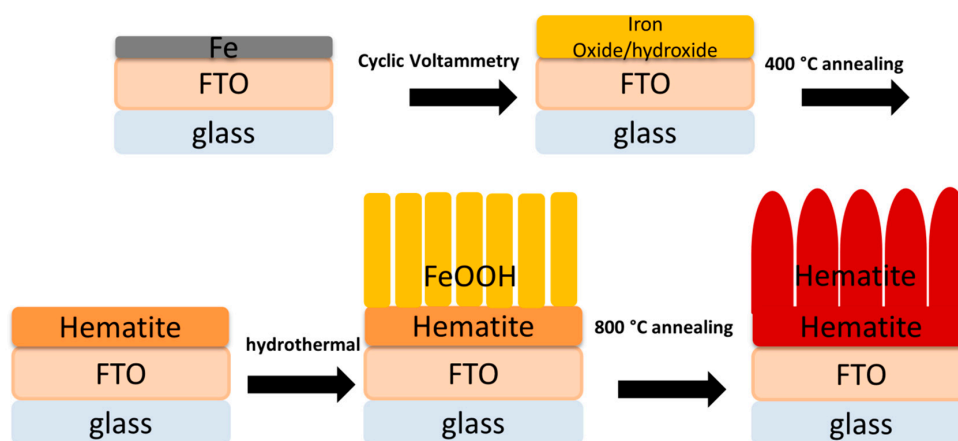


**Figure 2.** Schematic of the fabrication of the photoanodes with a hematite nanorod layer on hematite coated FTO substrate.

## 2.2. Zn-Co LDH Treated Samples

Zn-Co layered double hydroxides were prepared as described in an earlier work [35]. First, 0.3 mmol cobalt nitrate hexahydrate and 0.15 mmol zinc nitrate hexahydrate were added to 2.4 mmol urea and instantly dissolved in 10 mL DI water. Then, the solution was mixed with 40 mL ethylene glycol. Subsequently, the above solution was placed into a microwave (750 W) to be irradiated for 10 min with 30 s on and off interval, and then cooled naturally. After washing and drying, the product was dispersed in deionized water and sonicated for 10 min. Finally, the FTO samples without and with the blocking hematite layer which were covered by nanorod structure were immersed in the solution for 10 min, washed with DI water, and dried by nitrogen.

## 2.3. Morphological and Structural Characterization

A field emission scanning electron microscope (FE-SEM, Hitachi S4800, Tokyo, Japan) was used to investigate the morphology of the as-synthesized materials. The film thicknesses were measured using cross sectional imaging by SEM. X-ray diffraction patterns (XRD) were measured using X'pert Philips MPD diffractometer with a Panalytical X'celerator detector, Malvern Panalytical (Almelo, The Netherlands) to examine the structural properties of the materials. The measurements were carried out using graphite-monochromized  $\text{CuK}\alpha$  radiation (wavelength 1.54056 Å). X-Ray photoelectron spectroscopy (XPS, PHI 5600, Eden Prairie, MN, USA) was used for analysis of the chemical states and elemental composition of the samples. Additional compositional evaluation was carried out by time-of-flight secondary-ion mass spectrometer TOF-SIMS (ToF.SIMS 5 instrument), Ion-ToF GmbH, Münster, Germany. Positive SIMS spectra were taken.

## 2.4. Photoelectrochemical (PEC) Measurements

Photoelectrochemical measurements were carried out in 1 M KOH (pH 13.5) solution as an electrolyte using a solar simulator source (300 W Xe with optical filter) providing AM 1.5 (100  $\text{mW}/\text{cm}^2$ ) illumination. A three-electrode cell was used with the FTO/hematite sample as a photoanode (working electrode), Ag/AgCl (3 M KCl) as a reference electrode and a platinum foil as a counter electrode. Photocurrent versus voltage (I-V) curves were recorded by scanning the potential from  $-0.4$  to  $0.7$  V (vs. Ag/AgCl) at a scan rate of 2 mV/s using a Jaisle IMP 88 PC potentiostat. The light was chopped

off and on every 20 mV. The recorded potentials versus Ag/AgCl were converted to the reversible hydrogen electrode (RHE) scale using the following equation:

$$E_{\text{RHE}} = E_{\text{Ag/AgCl}} + 0.059 \text{ pH} + E_{\text{Ag/AgCl}},$$

where  $E_{\text{Ag/AgCl}}$  is the measured potential, and  $E_{\text{Ag/AgCl}} = 0.209 \text{ V}$  at  $25 \text{ }^\circ\text{C}$  for an Ag/AgCl electrode in 3 M KCl.

Incident photocurrent conversion efficiencies (IPCE) were measured at 0.5 V vs. Ag/AgCl in 1 M KOH recorded in 5 nm steps from 700 to 300 nm. Electrochemical impedance spectroscopy (EIS) measurements were performed from 100 KHz to 0.01 Hz at 1.23 V vs. RHE with amplitude of 10 mV using 369 nm LED light source at the 3-electrode set-up. Intensity-modulated photocurrent spectroscopy (IMPS) measurements were performed with 369 nm LED light in 1 M KOH.

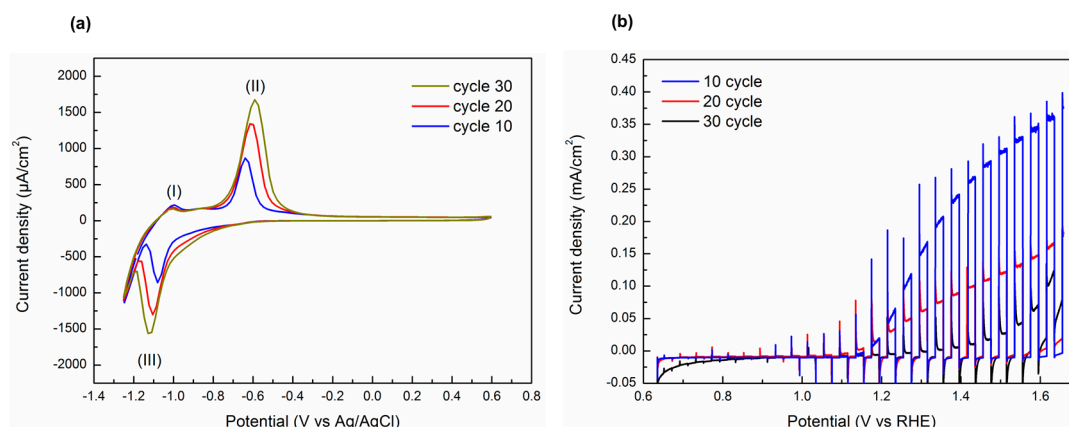
### 3. Results and Discussion

Figure 3a shows cyclic potential scans measured on FTO coated with a 30 nm thin iron film for 10, 20 and 30 cycles. The CV curves were obtained by polarizing the working electrode in the potential window of water stability in 0.1 M NaOH, i.e., the window was set to minimize  $\text{H}_2$  and  $\text{O}_2$  evolution. The mechanism of oxide film formation on metallic iron in alkaline solutions by cyclic voltammetry is well described in literature [45]. Starting from the open circuit potential (OCP) in the anodic direction, as the potential reaches peak (I) and (II), oxidation of the metallic iron takes place with formation of Fe(III) oxide (peak II). In the cathodic direction this oxide layer is converted to a Fe(II) oxyhydroxide layer (peak III). This Fe(II) oxyhydroxide layer is porous and thus allows in the next anodic cycle again the formation of an anodic high field oxide film underneath the hydroxide [45], i.e., in the subsequent cycle in the anodic direction, Fe(II) oxide is formed underneath the porous oxyhydroxide layer (at peak I). When the potential reaches peak II, Fe(II) is oxidized to Fe(III), and thus the oxide layer is thickened by one increment. In the subsequent cycle in the cathodic direction, the entire Fe(III) oxide layer is reduced to porous Fe(II) oxide/hydroxide. Thus, with each cycle, a steadily increasing thickness of a porous Fe-oxyhydroxide is formed. This process is well documented by in situ XANES measurements that not only follow the red/ox switching but also confirm thickening of the oxide/hydroxide film in each cycle [45].

A series of experiments were carried out with initial Fe layers of different thickness. For our purpose the best results were obtained for layers that were 30 nm thick and cycled 20 times. While a full conversion of the samples is reached between 20 to 30 cycles, the best photocurrent results were obtained for samples cycled 20 times (see Figure 3b), i.e., for samples that had a very thin remaining Fe layer on the surface. One may note that during the cycling, the anodic and cathodic peaks shift to higher and lower potentials, respectively. This can be ascribed to thickening of the film, resulting in an increase of the ohmic drop [46,47].

The CV measurements were carried out in the potential range of water stability. In the literature, by polarizing the iron sheet with a starting potential of  $-1.4 \text{ V. SCE}$  (i.e.,  $-1.444 \text{ V vs. Ag/AgCl}$ ), extensive hydrogen evolution occurs and a second cathodic peak in the CV appears. In other words, if the potential at the surface of the layer reaches the hydrogen evolution equilibrium potential, hydrogen is formed [48]. To suppress hydrogen evolution, the potential scans were started at  $-1.256 \text{ V}$  [49]. Strong hydrogen evolution during cycling can lead to layer detachment from the substrate.

Figure 3b shows photocurrent voltage curves of different thick oxide layers after annealing at  $400 \text{ }^\circ\text{C}$  in air for 1 h. The reason for the highest photocurrent density for the 20 times cycled sample is that for 30 cycles, adhesion of the layer to the substrate is lost during annealing. In other words, the thin metal layer remaining after 20 cycles provides after thermal conversion an optimum adhesion layer, without blocking charge transfer to the substrate.



**Figure 3.** (a) Cyclic voltammograms of Fe sputtered layer in 0.1 M NaOH (sweep rate 5 mV/s), (b) J-V curves with chopped light illumination for hematite thin oxide film prepared with 10, 20 and 30 CV cycles.

Figure 4a and b show the top view and cross section of the optimized sputtered iron layer used in this work. As seen in Figure 4b, the thickness of the sputtered iron layer is initially about 30 nm. After conversion of this layer, the layer consists of dense iron-oxyhydroxide nano platelet structure with a thin underneath compact layer. The 93 nm nanoplatelet structure is vertically aligned on the substrate. This layer was then converted to hematite by annealing at 400 °C for 1 h in air. The platelet structure with an underneath compact layer was stable after annealing Figure 4c,d, the compact layer was converted to compact oxide. This annealed layer was then used as the hematite blocking layer.

As shown in Figure 4f, hematite nanorods could be vertically grown on the blocking layer by the solution-based hydrothermal method described in the experimental section. The layer was subsequently annealed at 800 °C for 15 min to convert the FeOOH (of the rods) to hematite. Figure 4f shows that after 3 h of hydrothermal process, the nanorods are approximately 250 nm in length. A hydrothermal layer that was grown under the same conditions on plain FTO showed rods of 220 nm in length. This sample was taken as a reference sample in further experiments. The thickness of the nanorod layers can be changed by changing the nanorod growing time. As shown in Figure S1 (supporting information) and Figure 4f, the nanorods grown on the hematite blocking layer for 1, 3 and 9 h have average lengths of 180, 220 and 320 nm, respectively.

Figure 5 shows XRD patterns of the optimized blocking layers which were prepared by cyclic voltammetry before and after annealing, and the XRD pattern with hydrothermal nanorods before and after annealing. The XRD pattern of the sputtered iron sample after optimized cyclic voltammetry shows characteristic peaks of FeOOH (Figure 5a). After annealing for 1 h at 400 °C in air, the pattern shows only characteristic peaks of hematite. This confirms the complete conversion of the FeOOH layer, which was formed by cyclic voltammetry, to hematite. The (110) hematite diffraction peak at  $2\theta = 35.8^\circ$  with highest intensity indicates that the hematite nanostructure has preferential growth orientation in the [110] direction [50]. According to previous reports, hematite has anisotropic conductivity with a conductivity along [110] direction that is 4 orders of magnitude higher than in the orthogonal plane, which makes charge transport and charge collection easier for these rods [51]. In other words, the preferential orientation of hematite shows better photocurrent because charge can be extracted more facile [11]. There is no difference between crystal structure of samples with and without blocking layer. The peaks at  $33.17^\circ$  and  $24.2^\circ$  are related to the underneath oxide layer.

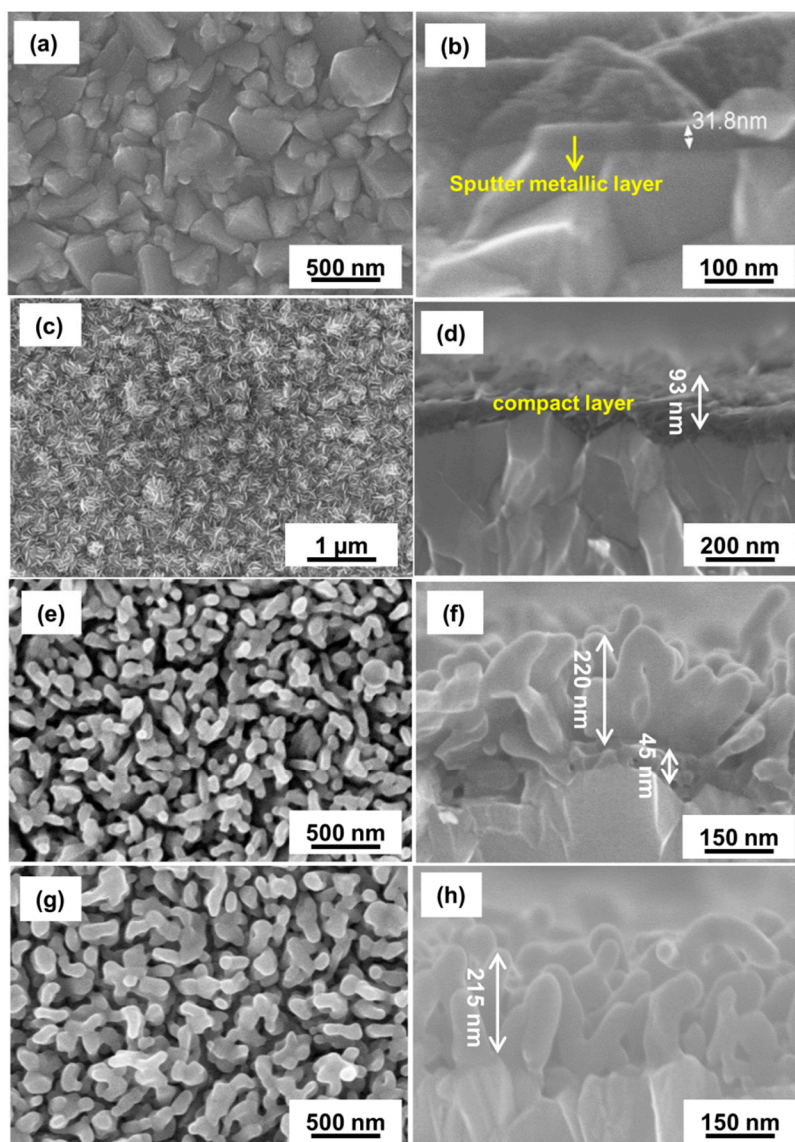


**Figure 4.** Top-view and cross sectional SEM images of (a,b) sputtered Fe layer, (c,d) hematite blocking layer, (e,f) hematite nanorods grown for 3 h with blocking layer, and (g,h) hematite nanorods grown for 3 h without blocking layer.

XPS survey spectrum in Figure S2 for annealed hydrothermal nanorods with and without blocking layer show that the structures are composed of Fe and O, with small traces of C. Figure 5b shows the high resolution XPS spectra for Fe for the above mentioned samples. Both samples show two distinct Fe  $2p_{1/2}$  and Fe  $2p_{3/2}$  peaks at 724.5 and 711.1 eV, respectively [52]. The satellite peak at 720 eV is characteristic of  $Fe^{3+}$  in  $Fe_2O_3$  [53]. Figure 5c shows the high-resolution O1s spectra: the peak at 530 eV corresponds to oxygen in the oxide structure, whereas the peak at 533 eV represents surface hydroxyl groups [54]. Hence, nanorods grown on the blocking layer samples show a higher amount of  $OH^-$  species than the reference samples. Figure S3a,b show XPS spectra of Zn and Co in ZnCo-LDH, respectively. ZnCo-LDH shows a Zn  $2p_{3/2}$  peak at 1021.7 eV, a Co  $2p_{1/2}$  peak at 797.7 eV and a Co  $2p_{3/2}$  peak at 782.1 eV, respectively in line with literature [55,56].

To additionally confirm the presence of ZnCo-LDH on hematite, we acquired TOF-SIMS spectra. From Figure S4, clearly Zn and Co peaks on the hematite nanorods can be identified.

The photocurrent response was measured in a 3-electrode cell using Ag/AgCl as a reference electrode in 1 M KOH under chopped solar simulator conditions. Figure 6a illustrates the photocurrent potential (J-V) response for hematite nanorods without blocking layer and without (H3) and with

Zn-Co OER catalyst (H3, Zn-Co), with blocking layer (BH3) and with both blocking layer and Zn-Co OER catalyst (BH3, Zn-Co).

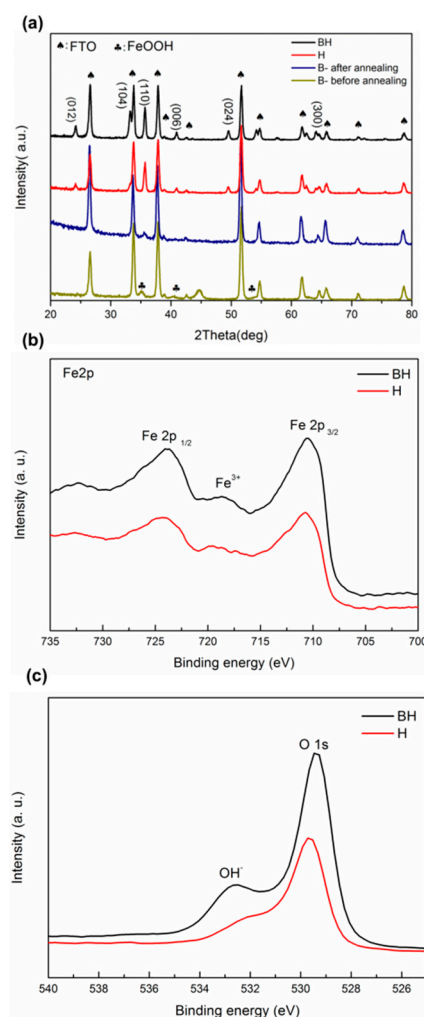


**Figure 5.** (a) XRD patterns for blocking layer (B) before and after annealing, nanorods without (H) and with blocking layer (BH). (b) XPS Fe 2p spectra of nanorods without (H) and with blocking layer (BH). (c) XPS O 1s spectra of nanorods without (H) and with blocking layer (BH).

Hydrothermal growth time for all the hematite nanorods for these measurements was 3 h. The photocurrent-voltage curves show an onset potential ( $V_{ON}$ ) of 0.9 and 0.86 V vs. RHE for the BH3 and H3 photoanodes, respectively. This undesired anodic shift for the samples with the blocking layer (BH3) is caused by the charge recombination in the hematite blocking layer at low potentials [57]. This undesired effect can be overcome using an  $O_2$  evolution catalyst, i.e., the onset potential could be shifted to a more cathodic potential (to 0.8 V vs. RHE) using a Zn-Co OER catalyst. The Zn-Co catalyst on control hematite nanorods (H3, Zn-Co) also shows the about 200 mV cathodic shift, similar to the (BH3/Zn-Co) photoanode as shown in Figure 6a.

However, the photocurrent plateau increases from 1 mA/cm<sup>2</sup> to 1.2 mA/cm<sup>2</sup> at 1.5 V vs. RHE for samples that carry a blocking layer. The high spikes at lower potentials also indicate that a better onset potential can be exploited when using an OER catalyst, as evidenced for curves measured using a Co-Zn LDH catalyst decoration.

One possible reason for increasing photocurrent characteristics of samples with blocking layer is that this layer becomes active as a hematite layer at higher onset potentials. Through the depletion layer, holes either trap in surface states or participate in water oxidation reaction. So in the synthesized layer, electron-hole recombination competes with charge separation and at low external bias the probability

of recombination is increased. By increasing the applied potential, this undesired recombination will be decreased and the beneficial effect dominates [52]. Evidently, by using the blocking layer, less FTO is exposed to the electrolyte and therefore less reaction sites for electron back injection are available, and also the dark (leakage) current is decreased [36].

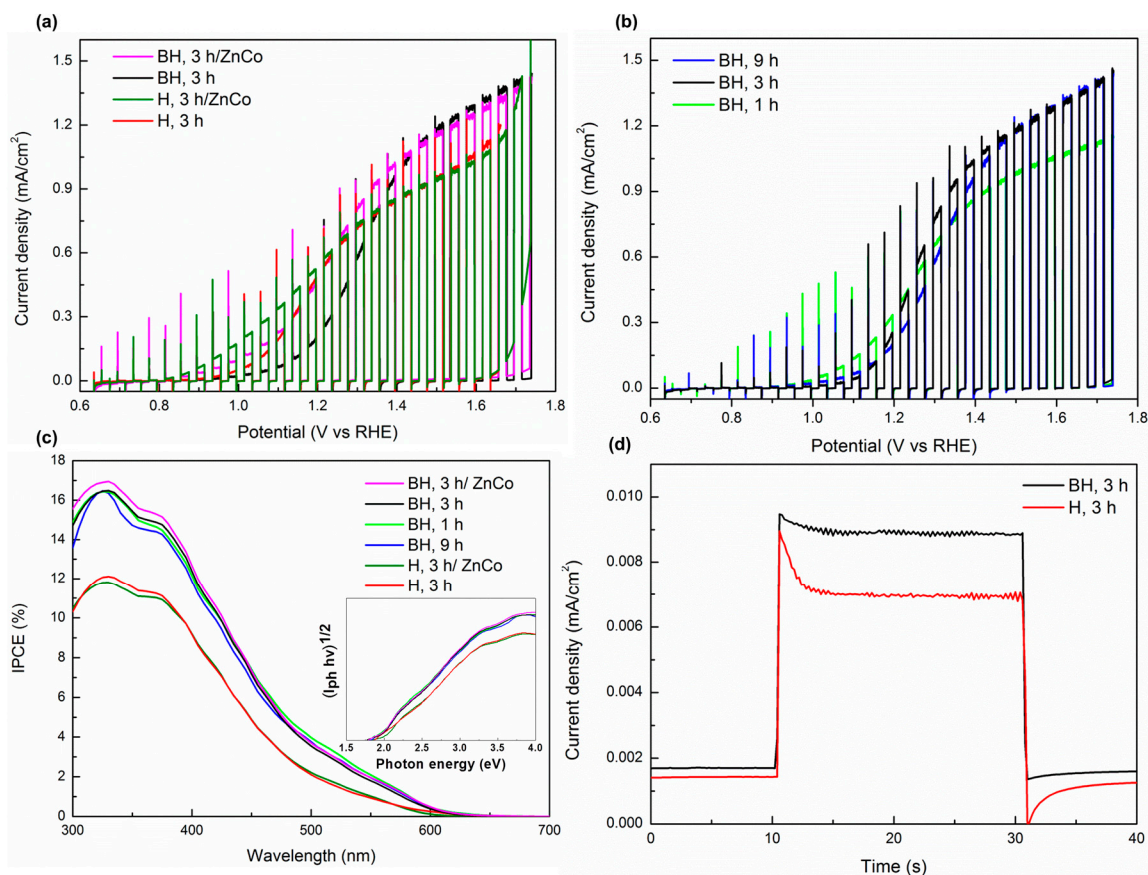


**Figure 6.** J-V curves with chopped light illumination measured at 0.6 to 1.7 V vs. RHE for: (a) reference sample, hematite nanorods (grown for 3 h) without blocking layer without (H) and with Zn-Co (H, ZnCo) and hematite nanorods (grown for 3 h) with blocking layer without (BH) and with Zn-Co (BH, ZnCo). (b) hematite nanorods with blocking layer grown for 1 h, 3 h and 9 h. (c) IPCE spectra for hematite nanorods grown for 1, 3 and 9 h and with Zn-Co decoration measured at 1.5 V vs. RHE, band gap determination from a  $(i_{ph} h\nu)^{1/2}$  vs. photon energy (eV) plot (inset). (d) transient photocurrent density of hematite with (BH) and without (H) blocking layer as a function of time at an applied bias of 1.5 V vs. RHE at 330 nm wavelength.

Figure 6b shows the photocurrent-potential curves for different length of hematite nanorods grown on blocking layer samples; hydrothermal growth times of hematite nanorods for this experiment were 1 h (BH1), 3 h (BH3) and 9 h (BH9). The nanorod samples prepared for 3 and 9 h show a better plateau current than the one prepared for 1 h. This directly correlates to light that can be absorbed by using longer nanorods [58]. However, the beneficial effect of increasing the length of the nanorods is limited, as hematite has a non-sufficient electrical conductivity.

In contrast to samples carrying a blocking layer, nanorod samples that were prepared for 1, 3 and 9 h on bare FTO, the plateau photocurrent did not change considerably by increasing the growth time (see Figure S5).

The presence of spikes in I-V curve is related to the recombination owing to the slow extraction of electron hole pairs (EHPs). Since the photogenerated EHPs can be quickly extracted by strong band-bending generated at high potential, the recombination of EHPs is suppressed and the magnitude of photocurrent spikes is diminished [59,60].

Figure 6c shows the incident photon to current efficiency (IPCE) of for all samples (without and with blocking layer, Zn-Co decorated, different nanorod lengths) measured at wavelengths from 300 to 700 nm at 1.5 V vs. RHE. The samples with blocking layers show a clear enhancement of the IPCE from 300 to 600 nm, and the highest IPCE value at 330 nm is about 17%. In comparison, the highest IPCE value for the hematite photoanodes grown on bare FTO with and without Zn-Co LDH at 330 nm are about 12%.

The band gap of the samples were obtained by plotting incident electron transition versus photon energy ( $(i_{ph}h\nu)^{1/2}$  vs.  $(h\nu)$ ) [61]. As seen in Figure 6c, for all samples the determined bandgap is ca. 1.9 eV. Figure 6d shows phototransients at 330 nm wavelength. During illumination, the photogenerated electrons and holes are separated and electron hole pairs recombine. As a result, transient photocurrent shows decay. At equilibrium (steady state), separation and recombination stabilize. After switching off the light, recombination occurs [54]. The spike which is observed when the light is switched off is related to back transfer of electrons from FTO to hematite [62]. Clearly, for the hematite blocking layer samples, recombination and electron back transfer are considerably suppressed.

Electrochemical impedance spectroscopy (EIS) was employed to investigate the kinetics of charge transport of hematite photoanodes grown on the blocking layer and decorated with the co-catalyst by the Zn-Co treatment in comparison to the reference sample; Nyquist curves of EIS experiments under illumination are shown in Figure 7a. Clearly, the charge transfer resistance for the blocking layer hematite photoanode with the Zn-Co catalyst is reduced as compared to the reference sample [53,63]. IMPS test was carried out to investigate charge transport behavior. The electron transient time can be calculated from semicircles which show imaginary current versus real current [54]. The transport time constant can be associated with photogenerated electrons transferring from the electrode to the back contact. As seen in Figure 7b, faster electron transport kinetics are observed for the blocking layer hematite photoanode with the Zn-Co catalyst, than for the reference sample (nanorods grown on plain FTO without the blocking layer and no co-catalyst decoration).

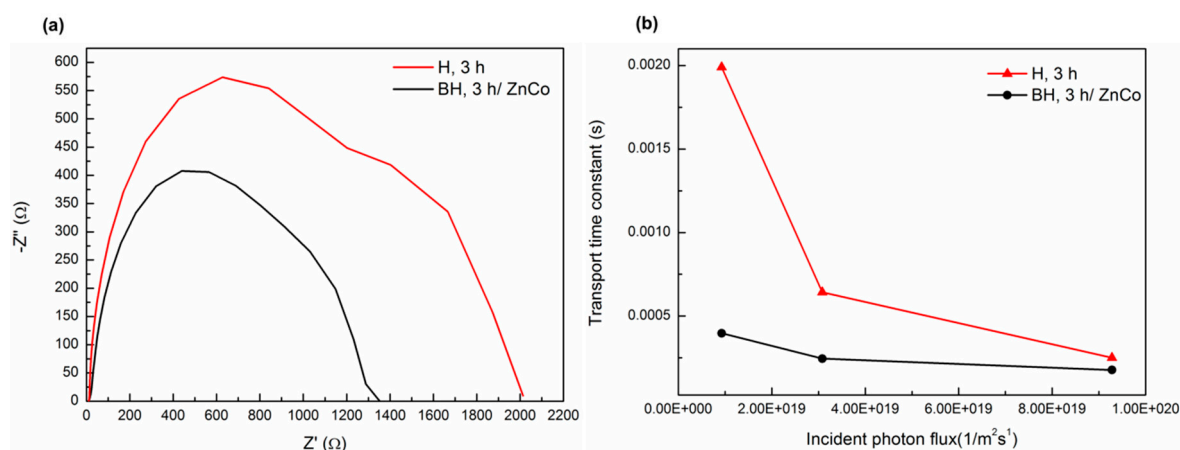


**Figure 7.** (a) EIS analysis (nyquist plots) of hematite nanorods grown for 3 h on plain FTO (H) and hematite nanorods with blocking layer and Zn-Co (BH, ZnCo) under 369 nm LED source at 1.2 V vs. RHE. (b) Intensity modulated photocurrent spectra (IMPS) of the samples.

#### 4. Conclusions

The work demonstrates a new approach to fabricate a nanostructured hematite photoelectrode with a blocking layer on FTO, where holes can recombine with back injected electrons before reaching the semiconductor- electrolyte interface. The layer of hematite that covers the FTO acts as a blocking layer to reduce the back injection of electrons from the FTO. Therefore, holes can reach the surface more efficiently and participate in oxygen evolution reaction [36,42,64,65]. Here we use a thin film of metallic iron coated on FTO that can be fully converted into an iron oxide/hydroxide layer by cyclic

voltammetry. This oxide/hydroxide can be further converted to a plain hematite layer. This layer acts as a blocking layer in the hematite-anostructure-photoanode. We have demonstrated that FTO with a blocking layer still serves as an efficient substrate for growing hematite nanorods. After such an electrode is additionally modified with Zn-Co as oxygen evolution reaction catalyst, an onset potential of 0.8 V vs. RHE is found and the photoanode showed a photocurrent of 1.2 mA/cm<sup>2</sup> at 1.5 V vs. RHE under AM 1.5 illumination.

**Supplementary Materials:** The following are available online at <http://www.mdpi.com/2571-9637/2/1/11/s1>, Figure S1: Cross sectional SEM images of 1 h (a) and 9 h (b) prepared hematite nanorods on blocking layer. Corresponding hematite nanorod layers grown on bare FTO for 1 h (c) and 3 h (d); Figure S2. XPS survey spectra of hematite nanorods grown on bare FTO (red line, H) and hematite nanorods grown on the blocking layer covered FTO (black line, BH); Figure S3. (a) XPS Zn 2p<sub>3/2</sub> spectrum and (b) Co 2p spectrum of ZnCo-LDH. Figure S4. TOF-SIMS analysis of hematite nanorods (grown for 3 h) without blocking layer (a) with Zn-Co (H, Zn-Co), (b) without Zn-Co (H, Zn-Co). Figure S5. J-V curves with chopped light illumination for hematite nanorods grown for 1, 3 and 9 h on bare FTO measured at 0.6 to 1.7 V vs. RHE.

**Author Contributions:** All authors contributed to conceptualization, experimental and interpretation as well as drafting the manuscript.

**Funding:** We would like to acknowledge the ERC, the DFG, the Erlangen DFG cluster of excellence EAM, project EXC 315 (Bridge), the DFG funCOS and the Operational Programme Research, Development and Education-European Regional Development Fund, project no. CZ.02.1.01/0.0/0.0/15\_003/0000416 of the Ministry of Education, Youth and Sports of the Czech Republic for financial support.

**Acknowledgments:** We would like to acknowledge Helga Hildebrand for her assistance in the ToF-SIMS and XPS measurements.

**Conflicts of Interest:** The authors declare no conflict of interest.

## References

1. Sivula, K.; Le Formal, F.; Grätzel, M. Solar water splitting: progress using hematite ( $\alpha$ -Fe<sub>2</sub>O<sub>3</sub>) photoelectrodes. *ChemSusChem* **2011**, *4*, 432–499. [[CrossRef](#)] [[PubMed](#)]
2. Roy, P.; Berger, S.; Schmuki, P. TiO<sub>2</sub> nanotubes: Synthesis and applications. *Angew. Chem. Int. Ed.* **2011**, *50*, 2904–2939. [[CrossRef](#)] [[PubMed](#)]
3. Grätzel, M. Photoelectrochemical Cells. *Nature* **2006**, *414*, 338–344. [[CrossRef](#)] [[PubMed](#)]
4. Kin, J.Y.; Youn, D.H.; Kim, J.H.; Kim, H.G.; Lee, J.S. Nanostructures-preserved hematite thin film for efficient solar water splitting. *ACS Appl. Mater. Interfaces* **2015**, *7*, 14123–14129. [[CrossRef](#)]
5. Khan, M.E.; Khan, M.M.; Cho, M.H. Fabrication of WO<sub>3</sub> nanorods on graphene nanosheets for improved visible light-induced photocapacitive and photocatalytic performance. *RSC Adv.* **2016**, *6*, 20824–20833. [[CrossRef](#)]
6. Khan, M.E.; Khan, M.M.; Min, B.K.; Cho, M.H. Microbial fuel cell assisted band gap narrowed TiO<sub>2</sub> for visible light-induced photocatalytic activities and power generation. *Sci. Rep.* **2018**, *8*, 1723–1735. [[CrossRef](#)] [[PubMed](#)]
7. Grigorescu, S.; Lee, C.Y.; Lee, K.; Albu, S.; Paramasivam, I.; Demetrescu, I. Thermal air oxidation of Fe: Rapid hematite nanowire growth and photoelectrochemical water splitting performance. *Electrochem. Commun.* **2012**, *23*, 59–62. [[CrossRef](#)]
8. Gajda-Schranz, K.; Tymen, S.; Boudoire, F.; Toth, R.; Bora, D.K.; Calvet, W.; Gratzel, M.; Constable, E.C.; Braun, A. Formation of an electron hole doped film in the  $\alpha$ -Fe<sub>2</sub>O<sub>3</sub> photoanode upon electrochemical oxidation. *Phys. Chem. Chem. Phys.* **2013**, *15*, 1443–1451. [[CrossRef](#)]
9. Sivula, K.; Formal, F.L.; Grätzel, M. WO<sub>3</sub>-Fe<sub>2</sub>O<sub>3</sub> Photoanodes for water splitting: A host scaffold, guest absorber approach. *Chem. Mater.* **2009**, *21*, 2862–2867. [[CrossRef](#)]
10. Peerakiatkajohn, P.; Yun, J.H.; Chen, H.; Lyu, M.; Butburee, T.; Wang, L. Stable hematite nanosheet photoanodes for enhanced photoelectrochemical water splitting. *Adv. Mater.* **2016**, *28*, 6405–6410. [[CrossRef](#)]
11. Kay, A.; Cesar, I.; Grätzel, M. New benchmark for water photooxidation by nanostructured  $\alpha$ -Fe<sub>2</sub>O<sub>3</sub> films. *J. Am. Chem. Soc.* **2006**, *128*, 15714–15721. [[CrossRef](#)] [[PubMed](#)]
12. Rangaraju, R.R.; Panday, A.; Raja, K.S.; Misra, M. Nanostructured anodic iron oxide film as photoanode for water oxidation. *J. Phys. D Appl. Phys.* **2009**, *42*, 1–10. [[CrossRef](#)]

13. Barroso, M.; Mesa, C.A.; Pendlebury, S.H.; Cowan, A.J.; Hisatomi, T.; Sivula, K.; Grätzel, M.; Klug, D.R.; Durrant, J.R. Dynamics of photogenerated holes in surface modified  $\alpha$ -Fe<sub>2</sub>O<sub>3</sub> photoanodes for solar water splitting. *PANS* **2012**, *109*, 15640–15645. [[CrossRef](#)] [[PubMed](#)]
14. Yue, G.; Ni, H.W.; Chen, R.S.; Li, Y.W.; Li, J.H. Time-dependent growth of hematite ( $\alpha$ -Fe<sub>2</sub>O<sub>3</sub>) nanotube arrays produced by iron anodizing in ethylene glycol solution. *Adv. Mater. Res.* **2012**, *599*, 145–150. [[CrossRef](#)]
15. Zhang, Z.; Hossain, M.F.; Takahashi, T. Self-assembled hematite ( $\alpha$ -Fe<sub>2</sub>O<sub>3</sub>) nanotube arrays for photoelectrocatalytic degradation of azo dye under simulated solar light irradiation. *Appl. Catal. B Environ.* **2010**, *95*, 423–429. [[CrossRef](#)]
16. Liu, T.; Ling, Y.; Yang, Y.; Finn, L.; Collazo, E.; Zhai, T.; Tong, Y.; Li, Y. Investigation of hematite nanorod–nanoflake morphological transformation and the application of ultrathin nanoflakes for electrochemical devices. *Nano Energy* **2015**, *12*, 169–177. [[CrossRef](#)]
17. Wang, L.; Lee, C.Y.; Kirchgorg, R.; Hildebrand, H.; Müller, J.; Spiecker, E.; Schmuki, P. A significant cathodic shift in the onset potential of photoelectrochemical water splitting for hematite nanostructures grown from Fe-Si alloys. *Mater. Horizons* **2014**, *1*, 344–347. [[CrossRef](#)]
18. Wen, X.; Wang, S.; Ding, Y.; Wang, Z.L.; Yang, S. Controlled growth of large-area, uniform, vertically aligned arrays of  $\alpha$ -Fe<sub>2</sub>O<sub>3</sub> nanobelts and nanowires. *J. Phys. Chem. B* **2005**, *109*, 215–220. [[CrossRef](#)]
19. Vincent, T.; Gross, M.; Dotan, H.; Rothschild, A. Thermally oxidized iron oxide nanoarchitectures for hydrogen production by solar-induced water splitting. *Int. J. Hydrogen Energy* **2012**, *37*, 8102–8109. [[CrossRef](#)]
20. Li, S.; Cai, J.; Mei, Y.; Ren, Y.; Qin, G. Thermal Oxidation Preparation of Doped Hematite Thin Films for Photoelectrochemical Water Splitting. *Int. J. Photoenergy* **2014**, 1–6. [[CrossRef](#)]
21. Shinde, P.S.; Lee, H.H.; Lee, S.Y.; Lee, Y.M.; Jang, J.S. PRED treatment mediated stable and efficient water oxidation performance of the Fe<sub>2</sub>O<sub>3</sub> nano-coral structure. *Nanoscale* **2015**, *7*, 14906–14913. [[CrossRef](#)] [[PubMed](#)]
22. Chernomordik, B.D.; Russell, H.B.; Cvelbar, U.; Jasinski, J.B.; Kumar, V.; Deutsch, T.; Sunkara, M.K. Photoelectrochemical activity of as-grown,  $\alpha$ -Fe<sub>2</sub>O<sub>3</sub> nanowire array electrodes for water splitting. *Nanotechnology* **2012**, *23*, 1–9. [[CrossRef](#)] [[PubMed](#)]
23. Wheeler, D.A.; Wang, G.; Ling, Y.; Li, Y.; Zhang, J.Z. Nanostructured hematite: synthesis, characterization, charge carrier dynamics, and photoelectrochemical properties. *Energy Environ. Sci.* **2012**, *5*, 6682–6702. [[CrossRef](#)]
24. Rangaraju, R.R.; Raja, K.S.; Panday, A.; Misra, M. An investigation on room temperature synthesis of vertically oriented arrays of iron oxide nanotubes by anodization of iron. *Electrochim. Acta* **2010**, *55*, 785–793. [[CrossRef](#)]
25. Albu, S.P.; Ghicov, A.; Schmuki, P. High aspect ratio, self-ordered iron oxide nanopores formed by anodization of Fe in ethylene glycol/NH<sub>4</sub>F electrolytes. *Phys. Status Solidi RRL* **2009**, *3*, 64–66. [[CrossRef](#)]
26. Lucas-Granados, B.; Sánchez-Tovar, R.; Fernández-Domene, R.M.; García-Antón, J. Controlled hydrodynamic conditions on the formation of iron oxide nanostructures synthesized by electrochemical anodization: Effect of the electrode rotation speed. *Appl. Surf. Sci.* **2017**, *392*, 503–513. [[CrossRef](#)]
27. Lee, C.Y.; Wang, L.; Kado, Y.; Killian, M.S.; Schmuki, P. Anodic nanotubular/porous hematite photoanode for solar water splitting: substantial effect of iron substrate purity. *ChemSusChem* **2014**, *7*, 934–940. [[CrossRef](#)]
28. Wang, L.; Lee, C.Y.; Schmuki, P. Improved photoelectrochemical water splitting of hematite nanorods thermally grown on Fe-Ti alloys. *Electrochem. Commun.* **2014**, *44*, 49–53. [[CrossRef](#)]
29. Hiralal, P.; Unalan, H.E.; Wijayantha, K.G.U.; Kursumovic, A.; Jefferson, D.; MacManus-Driscoll, J.L.; Amaratunga, G.A.J. Growth and process conditions of aligned and patternable films of iron (III) oxide nanowires by thermal oxidation of iron. *Nanotechnology* **2008**, *19*, 1–7. [[CrossRef](#)]
30. Li, M.; Deng, J.; Pu, A.; Zhang, P.; Zhang, H.; Gao, J.; Hao, Y.; Zhong, J.; Sun, X. Hydrogen-treated hematite nanostructures with low onset potential for highly efficient solar water oxidation. *J. Mater. Chem. A* **2014**, *2*, 6727–6733. [[CrossRef](#)]
31. Yilmaz, C.; Unal, U. Single step synthesis of ( $\alpha$ -Fe<sub>2</sub>O<sub>3</sub>) hematite films by hydrothermal electrochemical deposition. *RSC Adv.* **2015**, *5*, 16082–16088. [[CrossRef](#)]
32. Annamalai, A.; Shinde, P.S.; Jeon, T.H.; Lee, H.H.; Kim, H.G.; Choi, W.; Jang, J.S. Fabrication of superior  $\alpha$ -Fe<sub>2</sub>O<sub>3</sub> nanorod photoanodes through ex-situ Sn-doping for solar water splitting. *Sol. Energy Mater. Sol. Cells* **2016**, *144*, 247–255. [[CrossRef](#)]

33. Bohn, C.D.; Agrawal, A.K.; Walter, E.C.; Vaudin, M.D.; Herzing, A.A.; Haney, P.M.; Talin, A.A.; Szalai, V.A. Effect of Tin Doping on  $\alpha$ -Fe<sub>2</sub>O<sub>3</sub> Photoanodes for Water Splitting. *J. Phys. Chem. C* **2012**, *116*, 15290–15296. [[CrossRef](#)]
34. Fu, Z.; Jiang, T.; Zhang, L.; Liu, B.; Wang, D.; Wang, L.; Xie, T. Surface treatment with Al<sup>3+</sup> on a Ti-doped  $\alpha$ -Fe<sub>2</sub>O<sub>3</sub> nanorod array photoanode for efficient photoelectrochemical water splitting. *J. Mater. Chem. A* **2014**, *2*, 13705–13712. [[CrossRef](#)]
35. Ahn, H.J.; Goswami, A.; Riboni, F.; Kment, S.; Naldoni, A.; Mohajernia, S.; Zboril, R.; Schmuki, P. Hematite photoanode with complex nanoarchitecture providing tunable gradient doping and low onset potential for photoelectrochemical water splitting. *ChemSusChem* **2018**, *11*, 1873–1879. [[CrossRef](#)]
36. Cho, I.S.; Han, H.S.; Logar, M.; Park, J.; Zheng, X. Enhancing Low-Bias performance of hematite photoanodes for solar water splitting by simultaneous reduction of Bulk, interface, and surface recombination pathways. *Adv. Energy Mater.* **2016**, *6*, 1–9. [[CrossRef](#)]
37. Cowan, A.J.; Barnett, C.J.; Pendlebury, S.R.; Barroso, M.; Sivula, K.; Grätzel, M.; Durrant, J.R.; Klug, D.R. Activation energies for the rate-limiting step in water photooxidation by nanostructured  $\alpha$ -Fe<sub>2</sub>O<sub>3</sub> and TiO<sub>2</sub>. *J. Am. Chem. Soc.* **2013**, *133*, 10134–10140. [[CrossRef](#)] [[PubMed](#)]
38. Steier, L.; Herraiz-Cardona, I.; Gimenez, S.; Fabregat-Santiago, F.; Bisquert, J.; Tilley, S.D.; Grätzel, M. Understanding the role of underlayers and overlayers in thin film hematite photoanodes. *Adv. Funct. Mater.* **2014**, *24*, 7681–7688. [[CrossRef](#)]
39. Cao, D.; Luo, W.; Feng, J.; Zhao, X.; Li, Z.; Zou, Z. Cathodic shift of onset potential for water oxidation on a Ti<sup>4+</sup> doped Fe<sub>2</sub>O<sub>3</sub> photoanode by suppressing the back reaction. *Energy Environ. Sci.* **2014**, *7*, 752–759. [[CrossRef](#)]
40. Hisatomi, T.; Dotan, H.; Stefik, M.; Sivula, K.; Rothschild, A.; Grätzel, M.; Mathews, N. Enhancement in the performance of ultrathin hematite photoanode for water splitting by an oxide underlayer. *Adv. Mater.* **2012**, *24*, 2699–2702. [[CrossRef](#)] [[PubMed](#)]
41. Abel, A.J.; Garcia-Torregrosa, I.; Patel, A.M.; Opananont, B.; Baxter, J.B. SILAR-deposited hematite films for photoelectrochemical water splitting: Effects of Sn, Ti, thickness, and nanostructuring. *J. Phys. Chem. C* **2015**, *119*, 4454–4465. [[CrossRef](#)]
42. Bouhjar, F.; Bessaïs, B.; Mari, B. Ultrathin-layer  $\alpha$ -Fe<sub>2</sub>O<sub>3</sub> deposited under hematite for solar water splitting. *J. Solid State Electrochem.* **2018**, *22*, 2347–2356. [[CrossRef](#)]
43. Liang, Y.; Enache, C.S.; van de Krol, R. Photoelectrochemical characterization of sprayed  $\alpha$ -Fe<sub>2</sub>O<sub>3</sub> thin films: Influence of Si doping and SnO<sub>2</sub> interfacial layer. *Int. J. Photoenergy* **2008**, *2008*, 739864. [[CrossRef](#)]
44. Hisatomi, T.; Brillet, J.; Cornuz, M.; Le Formal, F.; Tétreault, N.; Sivula, K.; Grätzel, M. A Ga<sub>2</sub>O<sub>3</sub> underlayer as an isomorphic template for ultrathin hematite films toward efficient photoelectrochemical water splitting. *Faraday Discuss.* **2012**, *155*, 223–232. [[CrossRef](#)]
45. Schmuki, P.; Büchler, M.; Virtanen, S.; Isaacs, H.S.; Ryan, M.P.; Böhni, H. Passivity of iron in alkaline solutions studied by in situ XANES and a laser reflection technique. *J. Electrochem. Soc.* **1999**, *146*, 2097–2102. [[CrossRef](#)]
46. Díaz, B.; Freire, L.; Montemor, M.F.; Nóvoa, X.R. Oxide film growth by CSV on AISI 316L: A combined electrochemical and analytical characterization. *J. Braz. Chem. Soc.* **2013**, *24*, 1246–1258. [[CrossRef](#)]
47. Amaral, S.T.; Martini, E.M.A.; Müller, I.L. An attempt of experimental separation of the potentiodynamic anodic peaks of iron in alkaline solutions and application of the ohmic model for passive film growth. *Corros. Sci.* **2001**, *43*, 853–879. [[CrossRef](#)]
48. Büchler, M. Alternating current corrosion of cathodically protected pipelines: Discussion of the involved processes and their consequences on the critical interference values. *Mater. Corros.* **2012**, *63*, 1181–1187. [[CrossRef](#)]
49. Duschek, K.; Uhlemann, M.; Schlörb, H.; Nielsch, K.; Leistner, K. Electrochemical and in situ magnetic study of iron/iron oxide films oxidized and reduced in KOH solution for magneto-ionic switching. *Electrochem. Commun.* **2016**, *72*, 153–156. [[CrossRef](#)]
50. Xi, L.; Tran, P.D.; Chiam, S.Y.; Bassi, P.S.; Mak, W.F.; Mulmudi, H.K.; Batabyal, S.K.; Barber, J.; Loo, J.S.C.; Wong, L.H. Co<sub>3</sub>O<sub>4</sub>-decorated hematite nanorods as an effective photoanode for solar water oxidation. *J. Phys. Chem. C* **2012**, *116*, 13884–13889. [[CrossRef](#)]
51. Ling, Y.; Wang, G.; Wheeler, D.A.; Zhang, J.Z.; Li, Y. Sn-doped hematite nanostructures for photoelectrochemical water splitting. *Nano Lett.* **2011**, *11*, 2119–2125. [[CrossRef](#)] [[PubMed](#)]

52. Wu, Y.H.; Guo, W.R.; Mishra, M.; Huang, Y.C.; Chang, J.K.; Lee, T.C. Combinatorial studies on wet-chemical synthesized Ti-doped  $\alpha$ -Fe<sub>2</sub>O<sub>3</sub>: How does Ti<sup>4+</sup> improve photoelectrochemical activity? *ACS Appl. Nano Mater.* **2018**, *1*, 3145–3154. [[CrossRef](#)]
53. Annamalai, A.; Sandström, R.; Gracia-Espino, E.; Boulanger, N.; Boily, J.F.; Mühlbacher, I.; Shchukarev, A.; Wågberg, T. Influence of Sb<sup>5+</sup> as a double donor on hematite (Fe<sup>3+</sup>) photoanodes for surface-enhanced photoelectrochemical water oxidation. *ACS Appl. Mater. Interfaces* **2018**, *10*, 16467–16473. [[CrossRef](#)] [[PubMed](#)]
54. Qiu, P.; Yang, H.; Yang, L.; Wang, Q.; Ge, L. Solar water splitting with nanostructured hematite: The role of annealing-temperature. *Electrochim. Acta* **2018**, *266*, 431–440. [[CrossRef](#)]
55. McDonald, K.J.; Choi, K.S. Photodeposition of co-based oxygen evolution catalysts on  $\alpha$ -Fe<sub>2</sub>O<sub>3</sub> photoanodes. *Chem. Mater.* **2011**, *23*, 1686–1693. [[CrossRef](#)]
56. Tang, D.; Han, Y.; Ji, W.; Qiao, S.; Zhou, X.; Liu, R.; Han, X.; Huang, H.; Liu, Y.; Kang, Z. A high-performance reduced graphene oxide/ZnCo layered double hydroxide electrocatalyst for efficient water oxidation. *Dalton Trans.* **2014**, *43*, 15119–15125. [[CrossRef](#)] [[PubMed](#)]
57. Segev, G.; Dotan, H.; Malviya, K.D.; Kay, A.; Mayer, M.T.; Grätzel, M.; Rothschild, A. High solar flux concentration water splitting with hematite ( $\alpha$ -Fe<sub>2</sub>O<sub>3</sub>) photoanodes. *Adv. Energy Mater.* **2016**, *6*, 1–7. [[CrossRef](#)]
58. Li, M.; Yang, Y.; Ling, Y.; Qiu, W.; Wang, F.; Liu, T.; Song, Y.; Liu, X.; Fang, P.; Tong, Y.; et al. Morphology and doping engineering of Sn-doped hematite nanowire photoanodes. *Nano Lett.* **2017**, *17*, 2490–2495. [[CrossRef](#)]
59. Guo, X.; Wang, L.; Tan, Y. Hematite nanorods Co-doped with Ru cations with different valence states as high performance photoanodes for water splitting. *Nano Energy* **2015**, *16*, 320–328. [[CrossRef](#)]
60. Tamirat, A.G.; Su, W.N.; Dubale, A.A.; Chen, H.M.; Hwang, B.J. Photoelectrochemical water splitting at low applied potential using a NiOOH coated codoped (Sn, Zr)  $\alpha$ -Fe<sub>2</sub>O<sub>3</sub> photoanode. *J. Mater. Chem. A* **2015**, *3*, 5949–5961. [[CrossRef](#)]
61. Wang, L.; Zhou, X.; Nguyen, N.T.; Schmuki, P. Plasmon-Enhanced Photoelectrochemical Water Splitting Using Au Nanoparticles Decorated on Hematite Nanoflake Arrays. *ChemSusChem* **2015**, *8*, 618–622. [[CrossRef](#)] [[PubMed](#)]
62. Wang, D.; Zhang, X.T.; Sun, P.P.; Lu, S.; Wang, L.L.; Wei, Y.A.; Liu, Y.C. Enhanced photoelectrochemical water splitting on hematite thin film with layer-by-layer deposited ultrathin TiO<sub>2</sub> underlayer. *Int. J. Hydrogen Energy* **2014**, *39*, 16212–16219. [[CrossRef](#)]
63. Deng, J.; Zhang, Q.; Feng, K.; Lan, H.; Zhong, J.; Chaker, M.; Ma, D. Efficient Photoelectrochemical Water Oxidation on Hematite with Fluorine-Doped FeOOH and FeNiOOH as Dual Cocatalysts. *ChemSusChem* **2018**, *11*, 3783–3789. [[CrossRef](#)] [[PubMed](#)]
64. Qin, D.D.; Tao, C.L.; In, S.I.; Yang, Z.Y.; Mallouk, T.E.; Bao, N.; Grimes, C.A. Facile solvothermal method for fabricating arrays of vertically oriented  $\alpha$ -Fe<sub>2</sub>O<sub>3</sub> nanowires and their application in photoelectrochemical water oxidation. *Energy Fuels* **2011**, *25*, 5257–5263. [[CrossRef](#)]
65. Yang, T.Y.; Kang, H.Y.; Jin, K.; Park, S.; Lee, J.H.; Sim, U.; Jeong, H.Y.; Joo, Y.C.; Nam, K.T. An iron oxide photoanode with hierarchical nanostructure for efficient water oxidation. *J. Mater. Chem. A* **2014**, *2*, 2297–2305. [[CrossRef](#)]

